

# **Final Report for Finite-Element Method (ME6124)**

## **Robot Arm Optimization**

By Kad Kook, Zachary Burkhardt, and Min Park

April 23, 2024

Professor: Dr. Raghu Pucha  
Teaching Assistant: Kaushik Godbole

# Table of Contents

I.	Introduction .....	2
II.	Objectives.....	3
III.	Modeling .....	4
	a. Geometry.....	4
	b. Materials .....	5
	c. Element Selection & Justification.....	9
IV.	Static Analysis .....	11
	a. Mesh Convergence .....	11
	b. Boundary Conditions.....	12
	c. Result .....	12
	d. Validation .....	17
	e. Design Optimization .....	18
V.	Thermal Analysis.....	19
	a. Component Isolation & Justification .....	19
	b. Mesh Convergence .....	20
	c. Boundary Conditions.....	22
	d. Result .....	23
	e. Validation .....	24
	f. Design Optimization .....	24
VI.	Additional Studies .....	28
	a. Dynamic Analysis .....	28
	b. Failure Studies .....	29
VII.	Conclusion .....	31
VIII.	Future Works .....	31
IX.	Submitted and Approved Proposal .....	33
X.	References .....	35

## ***I. Introduction***

In the era of Industry 4.0, numerous manufacturing companies are transitioning to smart factories that integrate physical systems with computer-controlled technologies [1]. These advanced systems are designed to dynamically adapt manufacturing processes based on data analysis. A pivotal element of these smart factories is the robotic arm, which is widely utilized in diverse manufacturing and assembly operations.

Robotic arms typically have a capacity that is proportional to their size: larger payloads require larger arms. For example, a robotic arm capable of lifting a 4 kg load may be as small as 601 mm [2], whereas an arm designed to lift 300 kg generally extends at least 3.9 m [3]. This presents a significant challenge, as many manufacturing facilities are constrained by stringent spatial limitations and may not be equipped to accommodate larger robotic arms that can manage the requisite payloads. Furthermore, in sectors such as Glass Production, Foundries and Forging, and Ceramics Manufacturing - where robotic arms are increasingly employed to enhance worker safety - these devices must demonstrate exceptional durability and effective operation at elevated temperatures. For instance, in the forging industry, robotic arms are required to handle workpieces weighing approximately 60 kg - a critical demand considering the harsh conditions prevalent in these sectors [4]. As demands on these kinds of robotic arms, there is considerable opportunity to optimize and enhance robotic arms to increase efficiency and reduce operational costs.

This report details the development of a robotic arm, beginning with the initial modeling of a basic design. We applied finite element analysis to assess the static and thermal characteristics of the model, validating our results to ensure accuracy. Our subsequent analyses focused on optimizing the robotic arm's design. Through these efforts, we identified that the most effective design modification involved creating a 30 mm horizontal and 200 mm vertical hole in Link 2 and utilizing Silicon Carbide. Moreover, to enhance the arm's capacity for handling high-temperature objects, we concluded that replacing the material of Link 4 with zirconia would yield the best results.

## ***II. Objectives***

The project aims to design a 3R robotic arm with overall dimensions under 1 meter, capable of lifting and transporting an object weighing 200 kg and a temperature of 500°C. The fundamental criterion for the design optimization is that the deformation of the end effector's position must not exceed 3 mm when subjected to the operational load. While satisfying this condition, to reduce both weight and cost, a hole will be introduced in one of the linkages. The arm will be optimized by adjusting the material of the linkage and the dimensions of the hole under load to find the ideal configuration that maximizes strength while minimizing cost. Various materials and hole sizes will be systematically analyzed across different configurations, and the results will be compared to determine the most suitable material and hole size for the arm. Additionally, the end effector of the arm will undergo a thermal load analysis to simulate the extreme conditions under which the arm might operate, thereby determining the optimal material for this component of the design. The minimum requirements for the materials used in Link 4 aim to ensure that the temperature of the lower part of Link 4 (the battery) does not increase by more than 500°C. This specification is crucial to maintaining operational integrity and safety under high-temperature conditions.

### III. Modeling

#### Geometry

The arm is composed of a base linkage, three beam linkages, and two plates functioning as a gripper at the end effector. The geometric configuration is depicted in Figure 1, with detailed dimensions provided in Table 1. Throughout the static analysis testing, modifications to the geometry were implemented. Initially, the base model featured no holes in the link and included a gripper mounted on the end effector. However, given that the end effector is replaceable and not the primary focus of the study, it was excluded from the static and dynamic analyses. Throughout the static analysis testing, modifications to the geometry were implemented.

Specifically, a rectangular hole was introduced in Link 2. The length of this hole was consistently maintained at 200 mm, while the width was varied during the analysis to determine the ideal dimensions that would minimize weight while maximizing strength. Widths of 20 mm, 30 mm, and 40 mm were tested in static analysis to optimize the design of the robotic arm. For the dynamic analysis, which assessed the feasibility of the robotic arm, a 30 mm hole was used. This size was chosen based on the optimal results obtained from the static analysis.

Furthermore, since the end effectors and Link 4 are the principal areas of concern in thermal analysis, only these components were isolated for detailed examination. This approach was adopted following the result that variations in hole size influenced the temperature of the bottom of Link 4 by less than 1%.

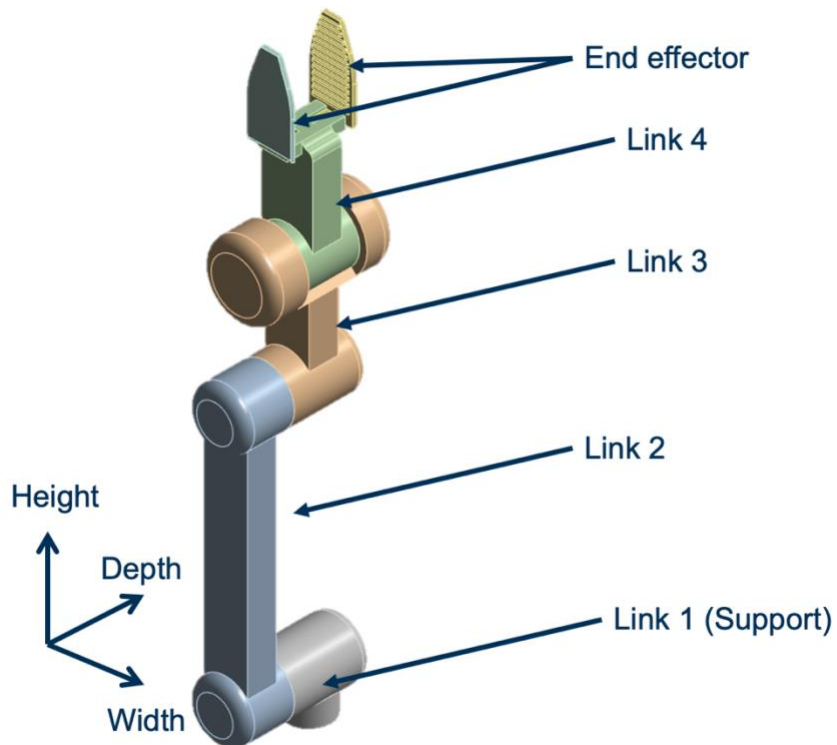


Figure 1. Major Components of a Standard Robotic Arm

Table 1. Dimensional Specifications of Robotic Arm Components: Links Excluding Joints and Overall Including Joints

Linkage	Height (mm)	Width (mm)	Depth (mm)
Link 1	60	60	60
Link 2	350	60	40
Link 3	150	60	40
Link 4	147.5	70	40
End Effector	120	60	5
Overall	817.5	100	200

## Material Properties

A variety of materials were evaluated to determine the optimal design for the robotic arm. Since Link 2 is the primary focus for optimization, the other linkages were standardized to structural steel for this analysis. Structural steel is a prevalent choice for robotic arm components due to its robust properties. The specific properties of the structural steel used are listed in table 2.

Table 2. Material Properties for Structural Steel

Material	Density [kg/m <sup>3</sup> ]	Young's Modulus [GPa]	Poisson's Ratio	Bulk Modulus [MPa]	Shear Modulus [MPa]	Yield Strength [MPa]	Thermal Conductivity [W/mK]
Structural Steel	7850	200	0.3	167	76.9	280	49.8

Additionally, its maximum service temperature is 350°C. These characteristics make structural steel a suitable base material for the non-optimized parts of the robotic arm, ensuring reliability under standard operational conditions. Figure 2 displays the phase diagram of structural steel, which illustrates the transformations that steel undergoes at various temperatures and compositions. Figure 3 depicts the S-N curve of the structural steel, providing insight into the material's fatigue life by correlating the stress amplitude with the number of cycles to failure.

To determine the most suitable materials for Link 2, a density versus yield strength graph was constructed using Edupack Granta, with filter lines highlighting materials exhibiting a density less than 8000 kg/m<sup>3</sup> and a density to Young's Modulus ratio exceeding 1. This targeted approach facilitated the selection of candidate materials for testing, as depicted in Figure 4. The materials that met these criteria, along with their respective properties, are detailed in Table 3.

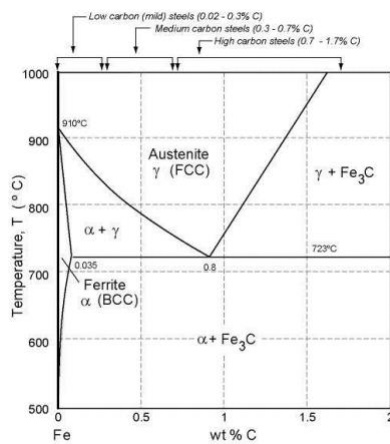


Figure 2. Phase Diagram of Structural Steel

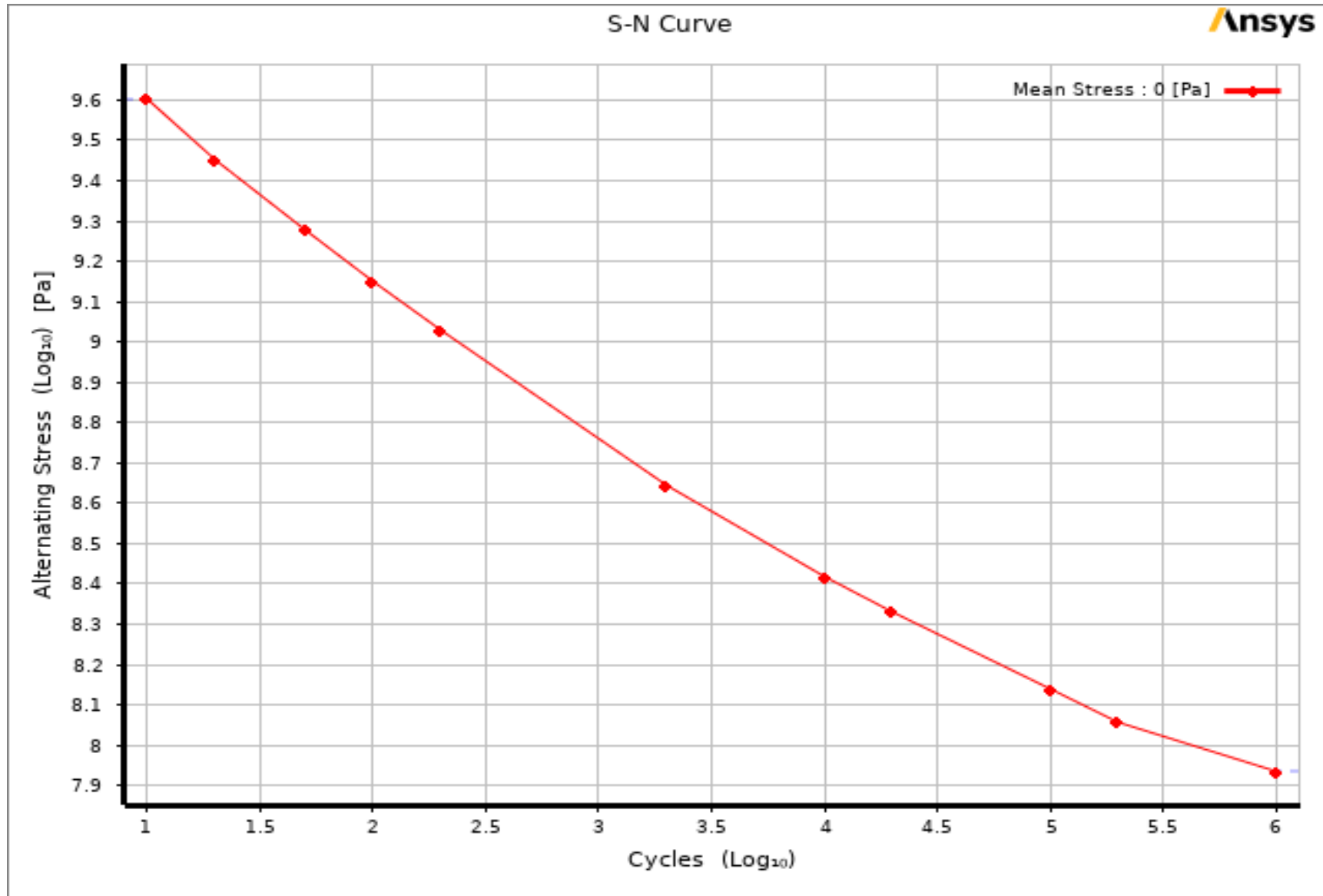


Figure 3. S-N Curve of Structural Steel

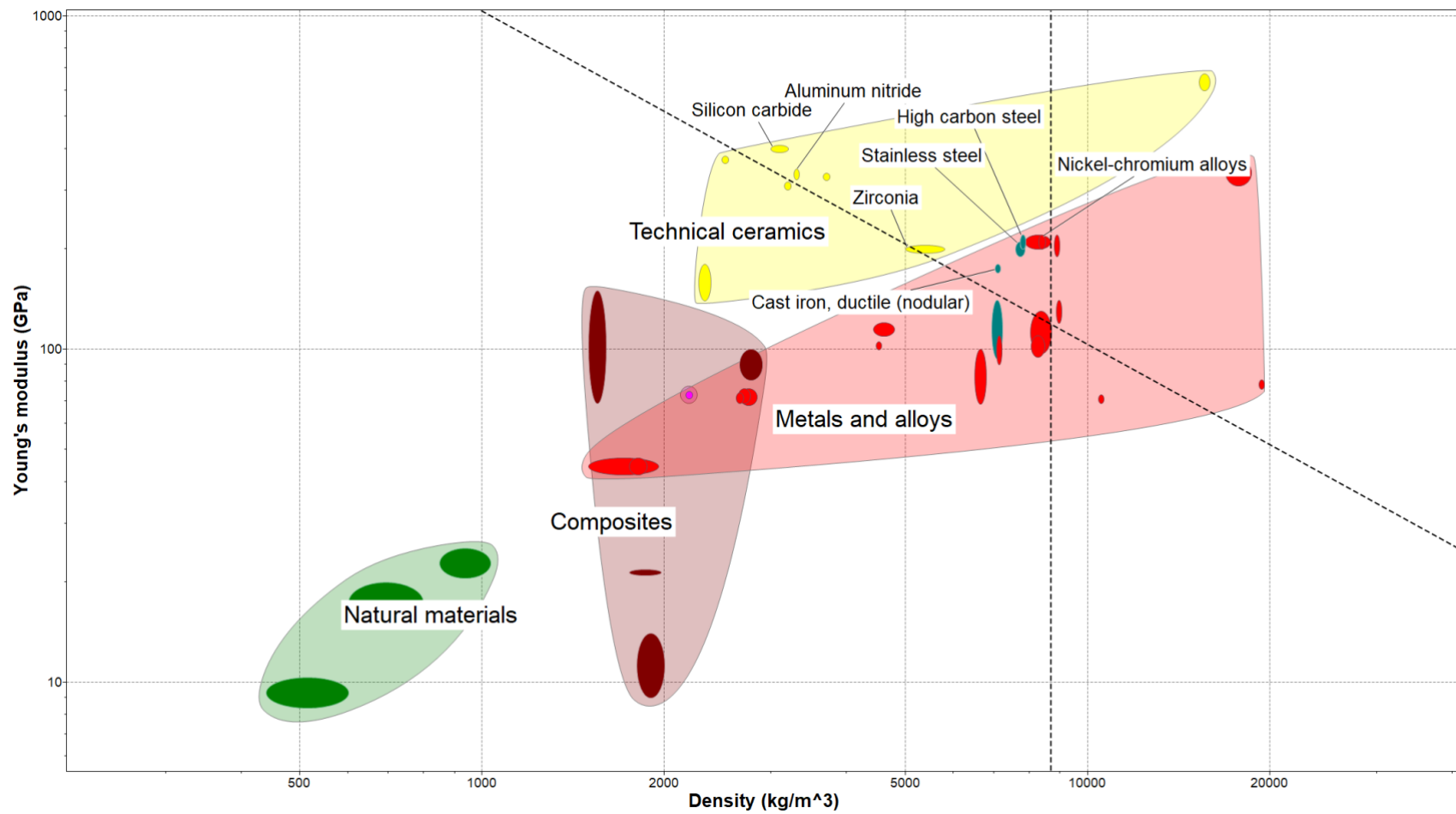


Figure 4. Graph of density vs Young's Modulus

Table 3. Comparative Table of Material Properties: Density, Young's Modulus, and Yield Strength

Material	Density [kg/m <sup>3</sup> ]	Young's Modulus [GPa]	Yield Strength [MPa]	Thermal Conductivity [W/mK]
Aluminum Alloy	2770	71	280	130
Stainless Steel	7750	193	205	15
High Carbon Steel	7800	210	678.5	47
Cast Iron	7000	170	275	31
Aluminum Nitride	3270	323	218	163
Silicon Carbide	3100	400	320	120
Zirconia	6095	138	230	16.7
Nickel Chromium	7750	210	412.5	17

## Element Selection and Justification

In the finite element analyses conducted, a Multizone mesh strategy was implemented in conjunction with a Hexa mapped mesh configuration for well-defined regions, while a program-controlled approach was utilized for surface mesh generation due to its complexity. For regions not amenable to structured meshing, a Hexa Core free mesh was employed. The Multizone technique enabled the partitioning of the arm's geometry into segments that are optimally mappable, thereby enhancing computational efficiency and the fidelity of the mesh. This partitioning was particularly vital in accommodating the discrete characteristics of each segment, from the mappable base to the more complex free-meshed articulations. Due to mesh generation constraints with manually specified types, the software's algorithm was relied upon to autonomously define the surface mesh. The Hexa Core method proved most efficacious for the free mesh segments, accommodating the intricate contours of the arm and ensuring the integrity of the results, especially at nodes subject to elevated stress. Figure 5 depicts the fully meshed robotic arm, highlighting the meshing techniques employed.

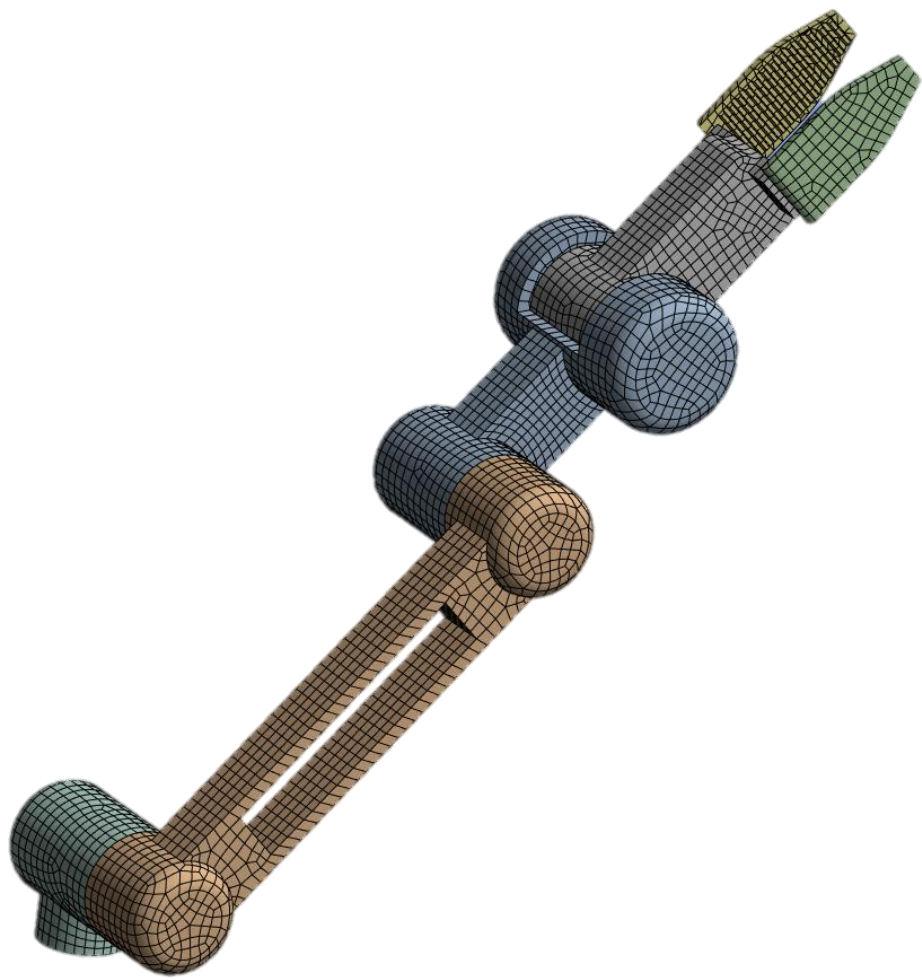


Figure 5. 3D Mesh Model of a Complete Robotic Arm Assembly

## IV. Static Analysis

### Mesh Convergence

Mesh convergence was conducted for physical analysis. Within this process, the average stress difference across six critical interest points—identified as locations of high stress—was monitored as the mesh element size was progressively reduced. The initial element size was set at 100 mm and was systematically decreased. The reduction process continued until the percentage difference in stress between successive mesh refinements fell below the threshold of 2.5%. Convergence was achieved when the transition from an 8 mm to a 6 mm element size did not exceed this predefined limit. Consequently, an element size of 8 mm was deemed appropriate for the physical analysis. The final mesh comprised 84,773 elements. Figure 6 illustrates the interesting points at which the average stress difference value was computed, while Figure 7 displays the mesh convergence graph for the physical studies.

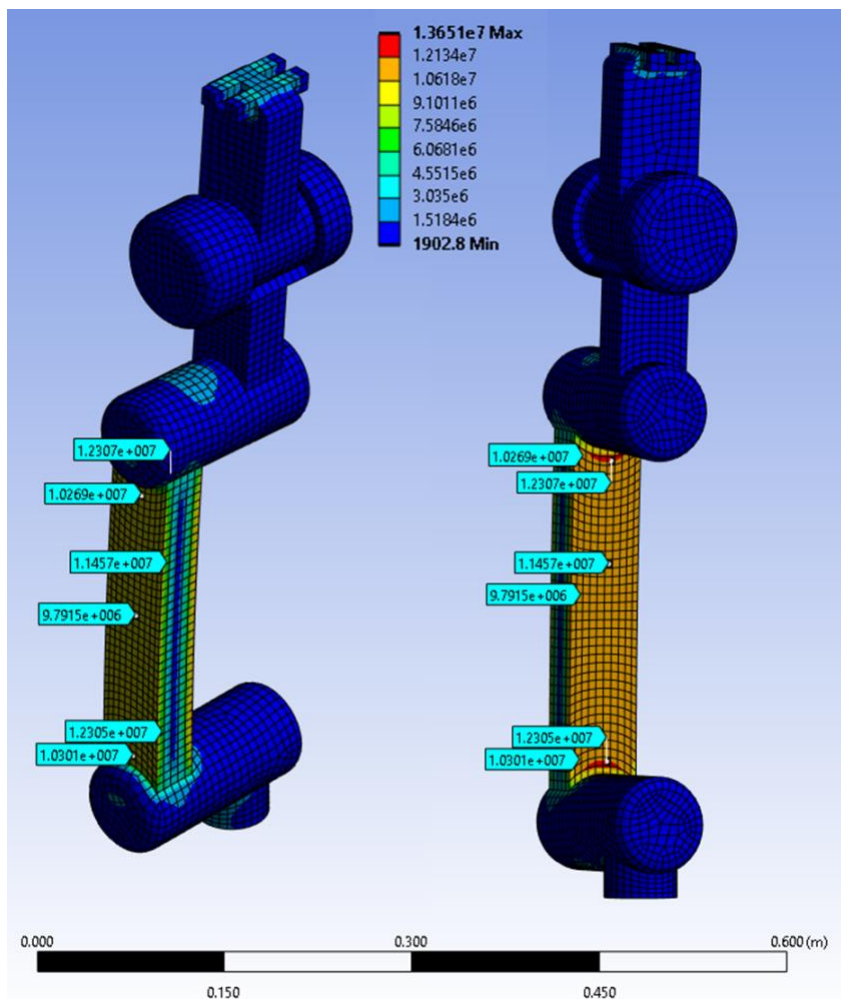


Figure 6. Illustration of Critical Mesh Convergence Points in a Robotic Arm

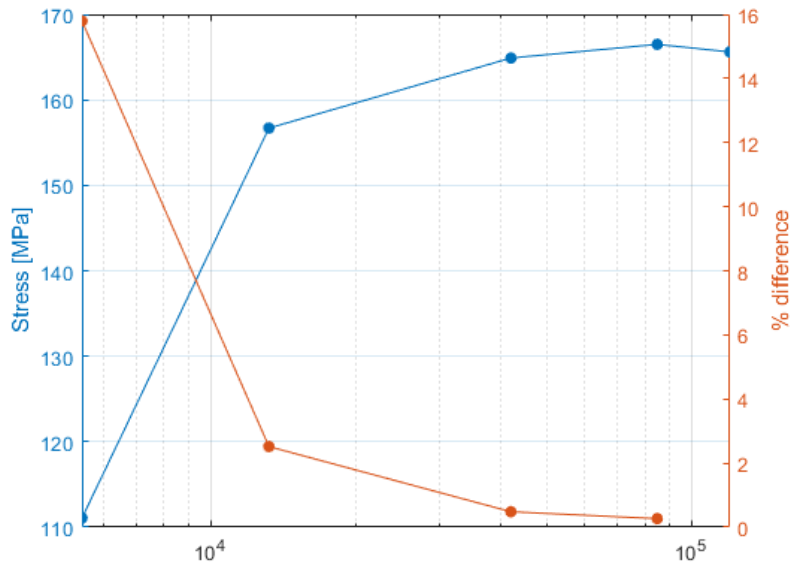


Figure 7. Graph of Mesh Convergence Results for Robotic Arm Physical Studies

## Boundary Conditions

For the static analysis, the base of the robotic arm was secured in position, emulating the real-world scenario where the arm is anchored to a table or floor. A force of 2000 N, corresponding to the weight of a 200 kg object under a gravitational acceleration of 10 m/s<sup>2</sup>, was exerted at the extremity of the arm.

## Result

Initially, the robotic arm was oriented vertically to simulate stress distribution on the front and back of the linkages. Boundary conditions were applied to mirror the constraints of a fixed position in a real-world application. The simulation revealed a maximum deformation at the end effector of only 0.4 mm (Figure. 8)—well below the permissible standard of 3 mm. This outcome indicated potential for material optimization, including the feasibility of incorporating a hole and using a material with lower stiffness than structural steel for the robotic arm.

Stress analysis identified Link 2 as the primary bearer of stress (Figure. 9), with the most significant stresses occurring at the rear, followed by the front and sides, in decreasing order. This distribution is likely due to the geometric design where the width exceeds the depth, affecting how stress is allocated across the structure. Given that Link 2 was identified as the primary stress bearer, prioritizing its design optimization was deemed essential. The initial step involved introducing a hole on the Link 2 to reduce weight without substantially compromising structural integrity. As the project progresses, further design optimizations for Links 3 and 4 may be considered. These additional modifications can be evaluated by replicating the initial simulations while simply altering the position of the support, ensuring a systematic assessment of each link's performance

under modified conditions, and facilitating targeted improvements throughout the robotic arm's structure.

Notably, the junctions where links and joints converge exhibited the highest stress concentration, measured at 12.305 MPa. Given that the stress levels within the robotic arm are well within safe operational limits—achieving a Factor of Safety (FoS) of 20.32, based on the yield strength of structural steel at 250 MPa—this suggests significant design robustness. This significant margin provides confidence in the current design and offers latitude for potential weight reduction and cost savings in subsequent iterations of the arm design.

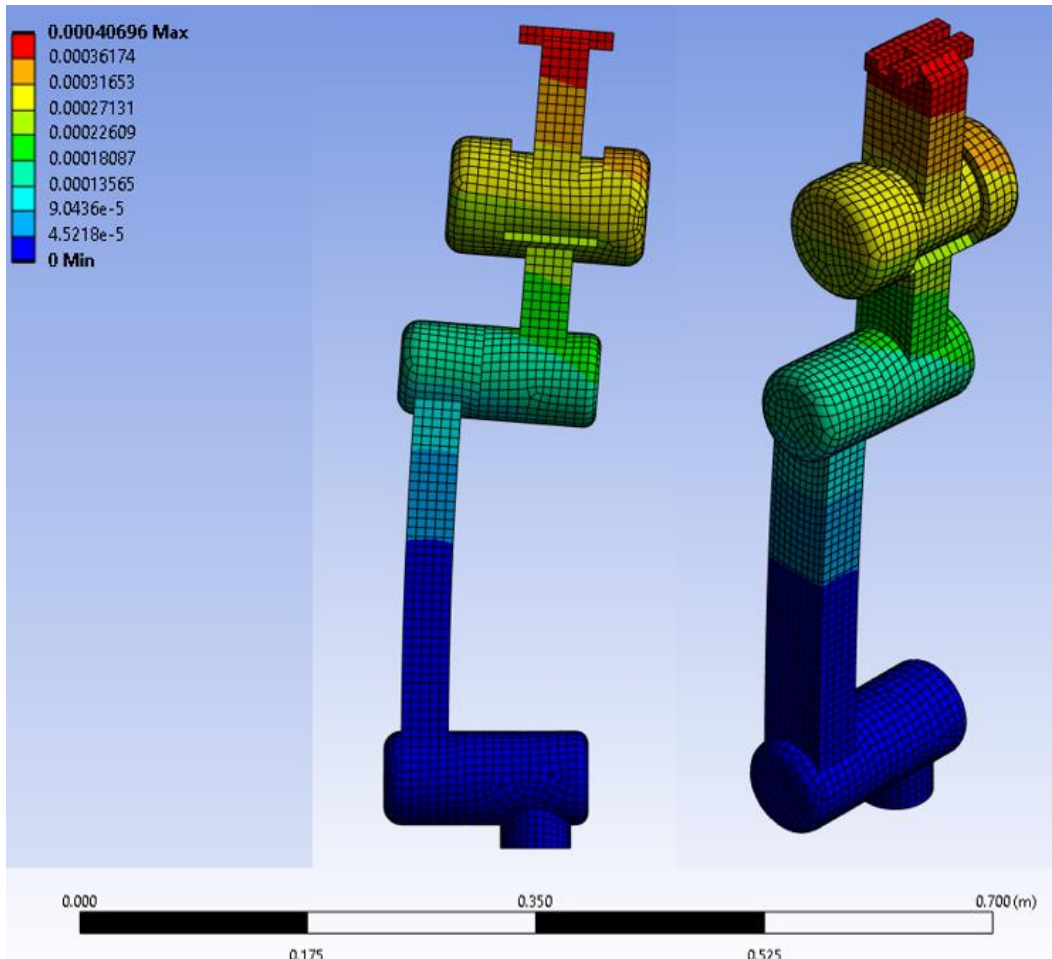


Figure 8. Total Deformation of a Vertically Oriented Robotic Arm Under 2kN Downward Force at End Effector

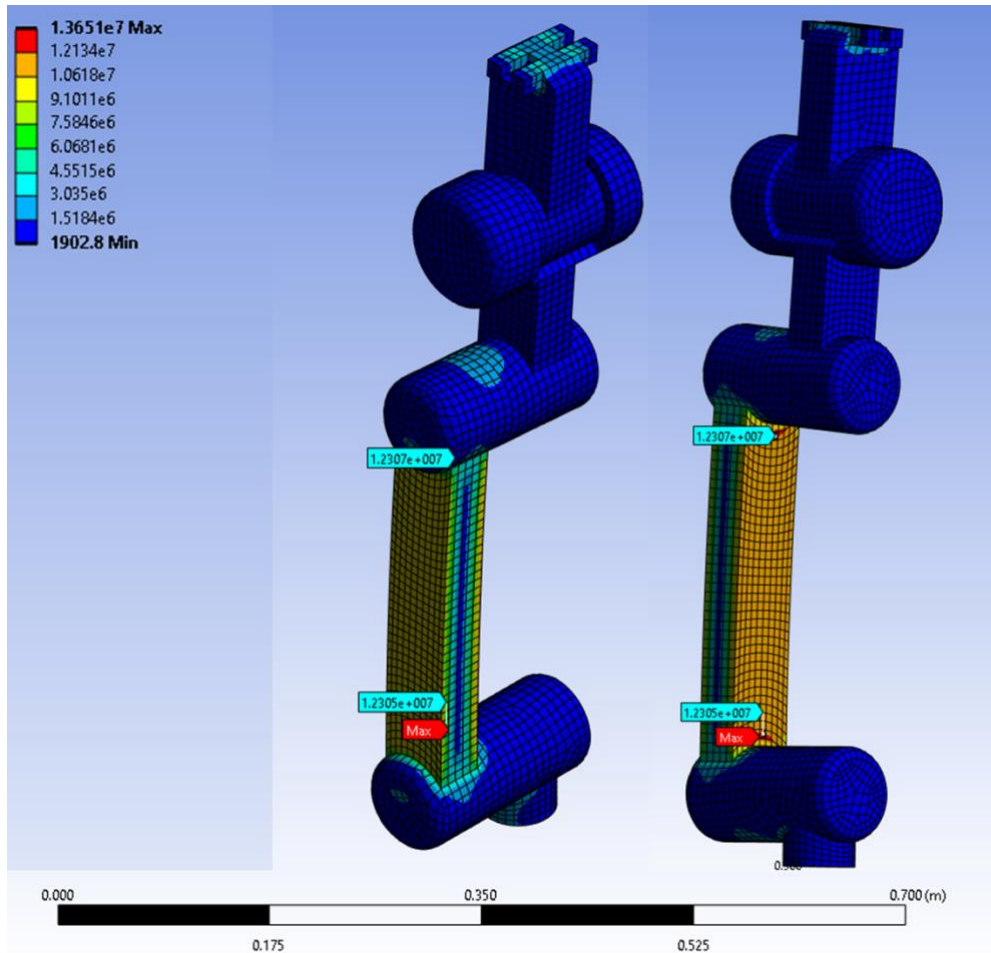


Figure 9. Equivalent Stress Distribution in a Vertical Oriented Robotic Arm Subjected to 2kN Downward Force at End Effector

In the second phase of testing, the robotic arm was positioned horizontally to simulate the stress distribution on the side of the linkage, using the same boundary conditions as in previous simulations. It was observed that structurally, the deformation was greater when the arm was oriented horizontally compared to vertically. This increased deformation is attributable to the greater horizontal distance between the support and the end effector, which results in a higher moment arm and thus greater moment forces for the same amount of applied load. Despite this, the deformation at the end effector was still within acceptable limits at 1.8 mm, less than the allowable 3 mm (as shown in Figure 10), indicating potential for further design enhancements.

The stress analysis revealed that Link 1 (the support) acted as the main stress transmitter (illustrated in Figure 11 and Figure 12). Among the other links, Link 2 was identified as the primary stress bearer. The highest stress concentration within the entire robot arm occurred at the joint where the support link and the joint meet, with a stress magnitude of 99.2 MPa. Given that the yield strength of the structural steel is 250 MPa, and thus the factor of safety (FoS) is 2.52, it was determined that design optimization for Link 1 was not necessary. Meanwhile, the greatest stress

concentration in Link 2 was observed at the connection between the link and its joint, with a stress value of 52.5 MPa. Considering the relatively high FoS of 4.76, it was concluded that there is ample scope for design optimization of Link 2.

Based on these findings, it was decided to proceed with the design optimization of Link 2 by introducing a hole on its side to reduce weight and by evaluating the potential for using a different material, thereby enhancing the arm's overall performance and efficiency.

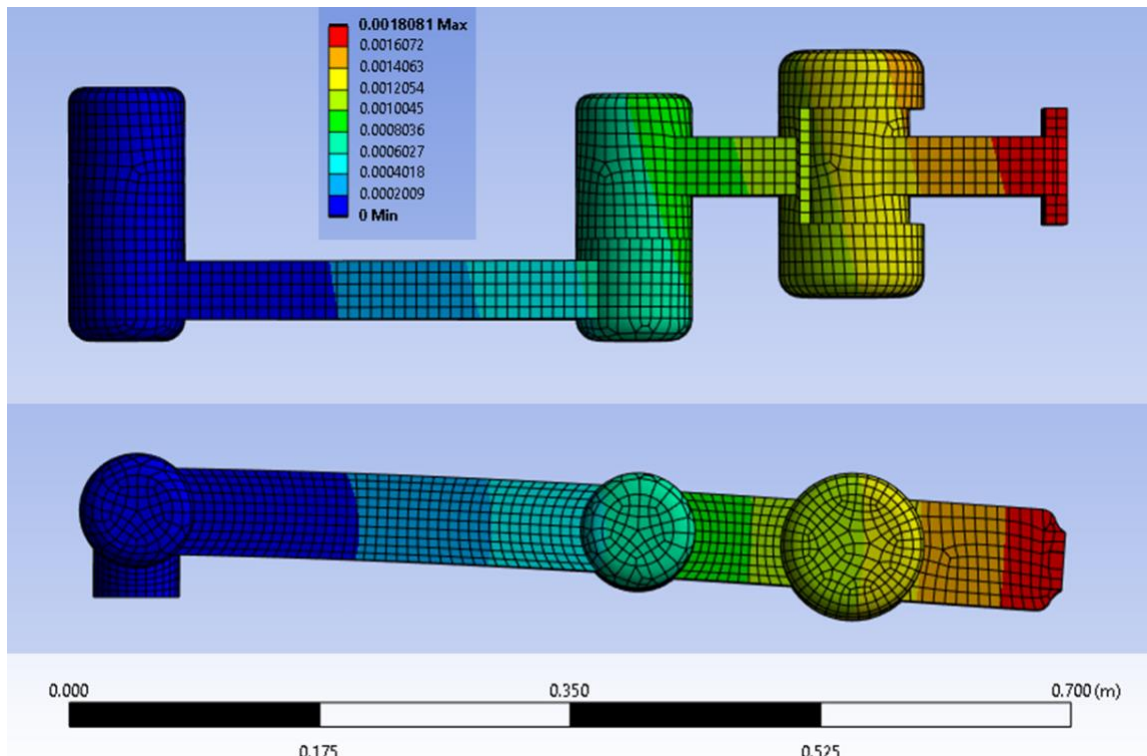


Figure 10. Total Deformation of a Horizontal Oriented Robotic Arm Under 2kN Downward Force at End Effector

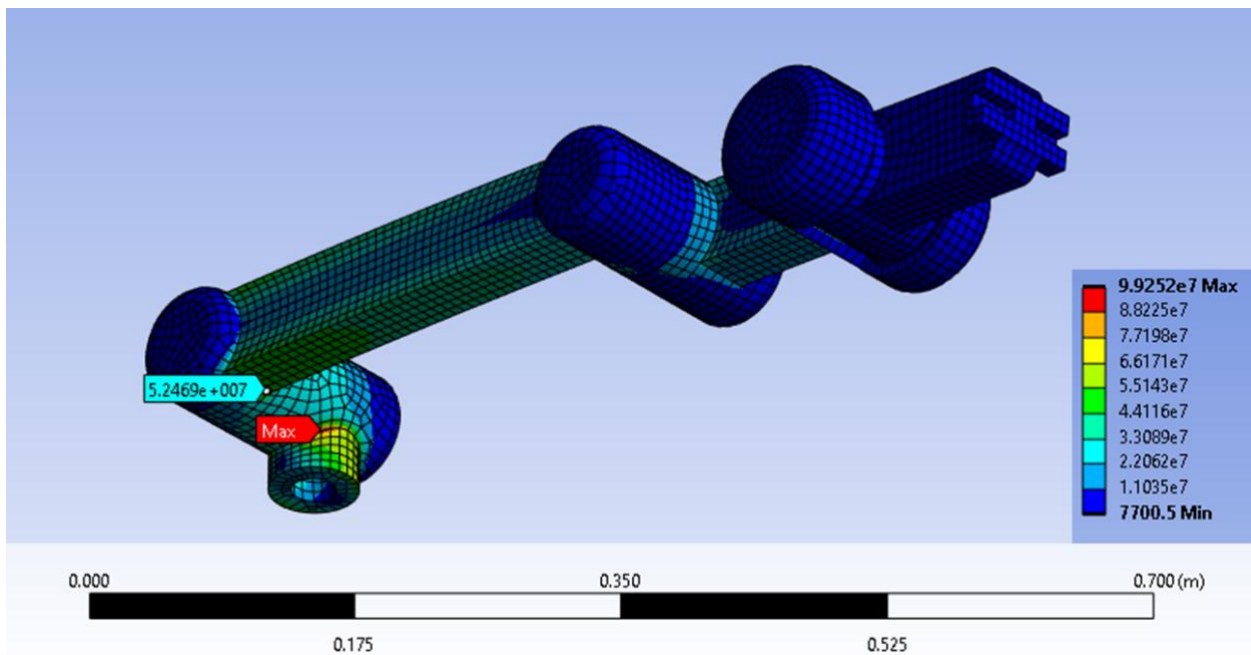


Figure 11. Equivalent Stress Distribution in a Horizontal Oriented Robotic Arm Subjected to 2kN Downward Force at End Effector

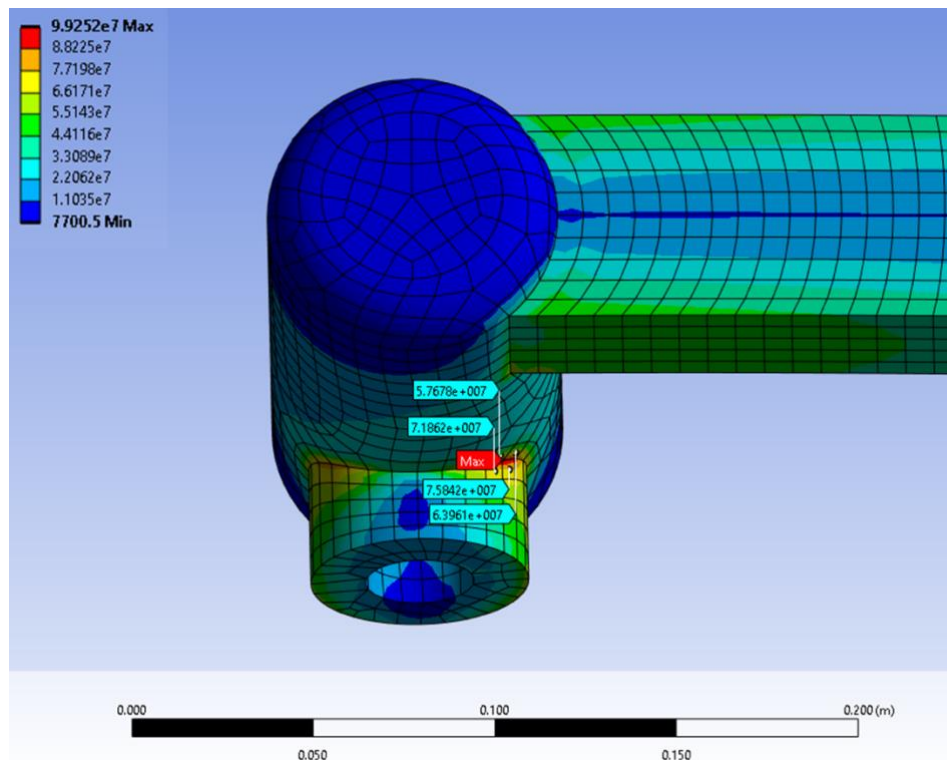


Figure 12. Detailed View of the Support and Joint Intersection Exhibiting Maximum Stress

## Validation

To validate the analysis on this arm, a simple stress calculation was performed on a vertical beam. This model represents the 90° orientation and the required dimensions and load can be seen in figure 13.

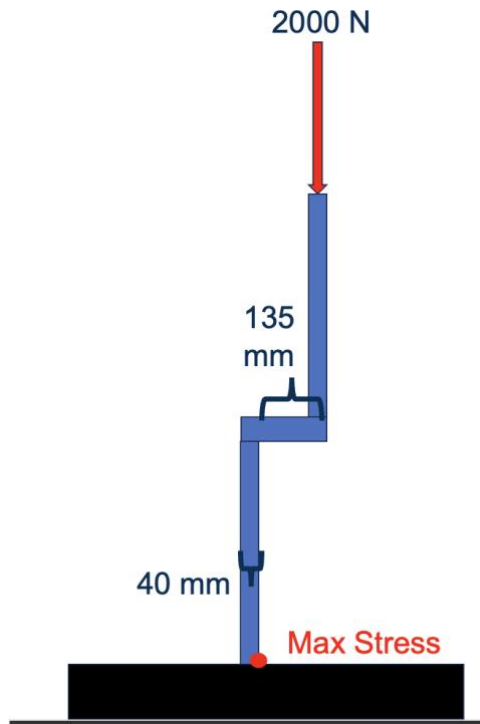


Figure 13. Simplified Free Body Diagram of Robotic Arm: Side View

The maximum stress will be located at the bottom of the arm and was analyzed found through bending moment analysis. Equations 1 through 4 detail the method used to determine the final bending stress of 16.9 MPa.

$$M = 2000 * .135 = 270 \text{ Nm}$$

Equation 1 – Bending moment

$$I = \frac{b * h^3}{12} = \frac{.06 * .04^3}{12} = 3.2 * 10^{-7} \text{ m}^4$$

Equation 2 – Area moment of inertia, where b is the base width of the linkage cross section and h is the height of the linkage cross section

$$c = \frac{1}{2} * h = .02 \text{ m}$$

Equation 3 – Centroidal distance

$$\sigma_{val} = \frac{M * c}{I} = \frac{270 * .02}{3.2 * 10^{-7}} = 16.9 \text{ MPa}$$

Equation 4 – Bending stress calculation

The maximum stress value found from the ANSYS simulation was 13.6 MPa, thus there is a 20% difference between the simulation and the calculation. Considering the significant simplification and the large factor of safety, this discrepancy is acceptable, and the design has been sufficiently validated.

## Design Optimization

Once the design had been validated, it was optimized to reduce the weight while still meeting the necessary criteria. A 200 mm long square hole was added to link 2 to reduce the weight, and 3 widths were tested – 20 mm, 30 mm, and 40 mm. 8 materials (see table 3 above) were tested at two different orientations (90° and 45°) for a total of 48 optimization simulations using the same 2000 N load. An example simulation can be seen in Figure 14.

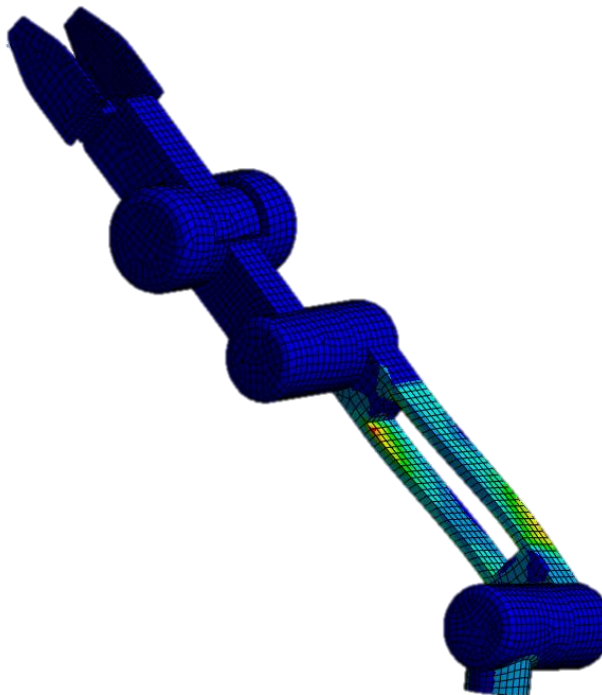


Figure 14. Optimization Simulation: aluminum alloy, 45°, 40 mm hole

The maximum stress and maximum deformation were calculated in each of these simulations, and the results were filtered to remove any simulations where the maximum stress exceeded the yield stress, or the maximum deformation exceeded 3 mm. Since the 90° simulations resulted in higher stresses with the same material and hole size than 45°, only these results were analyzed for optimization. After the filter was applied, only 6 simulations remained, the results of which

are detailed in table 4. Equation 5 was applied to rank the remaining choices, as a higher number means a more optimized balance between hole size (weight) and maximum deformation.

$$score = \frac{w}{d} * \frac{1}{1000}$$

Equation 5 – Scoring method for static design optimization results, where w is the width of the hole and d is the maximum deformation.

Table 4. Static Design Optimization Results

Config	Material	Hole Size (mm)	Max Equivalent (Von Mises) Stress - Pa	Max Deformation (mm)	Score	Ranking
90	SiC	30	132	1.91	15.7	1
90	SiC	40	303	2.64	15.2	2
90	SiC	20	126	1.36	14.7	3
90	Aluminum nitride	30	132	2.15	14.0	4
90	Aluminum nitride	20	107	1.52	13.2	5
90	High carbon steel	20	99.8	2.16	9.27	6

For the optimized design, linkage 2 will be made of silicon carbide and have a 200 mm by 30 mm hole created to reduce the weight. This optimized arm will be used for further analysis later in the design process.

## V. Thermal Analysis

### Component Isolation & Justification

Prior to conducting thermal analysis, specific components were isolated to enhance the efficiency of the simulations. We established several key assumptions:

- Assumption 1: The motor will operate normally when handling high-temperature objects if its temperature does not exceed a predefined threshold.
- Assumption 2: The motor installed in Link 4 operates at a higher temperature than those in other links due to its proximity to the heat source.
- Assumption 3: If the temperature variation within Link 4 is minor enough to be influenced by structural changes, then simulating only Link 4 and the end effector independently is sufficient.

The initial step involved measuring temperature changes near the Link 4 motor by adjusting the hole size in Link 2 under simulated conditions (500°C load applied to the end effector and an ambient temperature of 22°C). As illustrated in Figure X, temperatures increased nearer to the end effector. However, the impact of varying the hole size on the temperature near the Link 4 motor was minimal, with changes of less than 1% as shown in Figure 15.

These results validated Assumptions 2 and 3, allowing us to proceed with simulations focusing exclusively on Link 4 and the end effector.

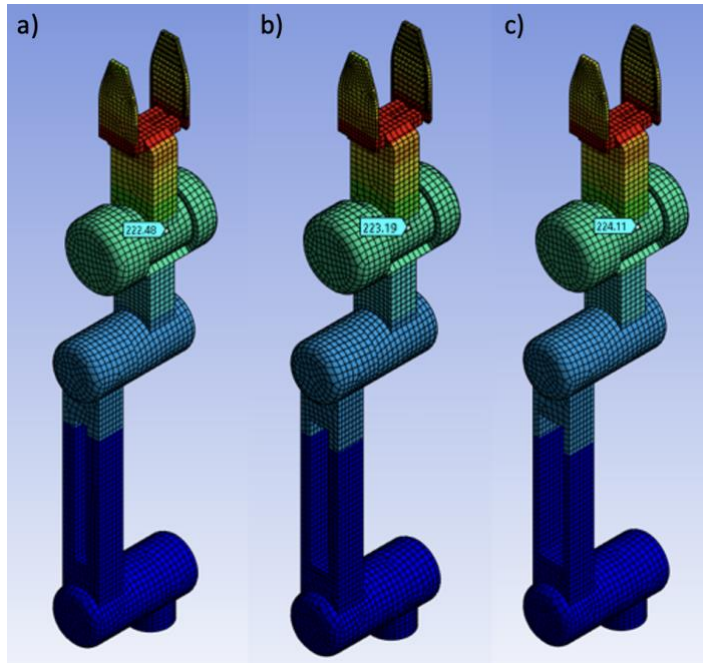


Figure 15. Comparison of Motor Temperature Across Different Hole Widths: 20mm (a), 30mm (b), and 40mm (c)

## Mesh Convergence

Mesh convergence was conducted for thermal analysis. During this process, the average difference in heat flux across four interest points—identified as critical for understanding the thermal behavior—was monitored as the mesh size was progressively reduced. Figure 16 illustrates the specific elements used for calculating the representative heat flux value. The initial mesh size was set at 100 mm and was systematically decreased. This reduction continued until the percentage difference in heat flux between successive mesh refinements fell below the threshold of 2.5%. Convergence was achieved when the transition from a 5 mm to a 4 mm mesh size did not exceed this predefined limit. Consequently, a mesh size of 5 mm was deemed appropriate for the detailed thermal analysis. Figure 17 displays that the mesh has adequately converged. The final mesh comprised 53,666 elements.

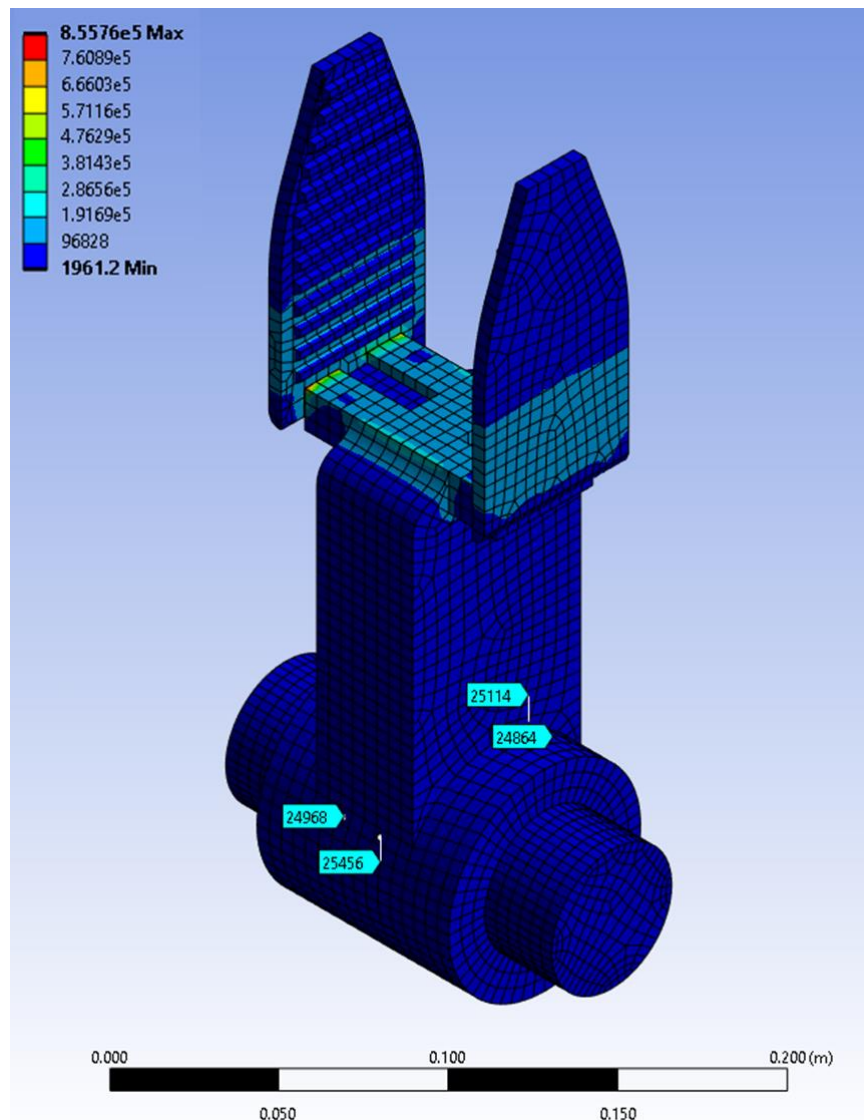


Figure 16. Illustration of Critical Mesh Convergence Points in the Link 4

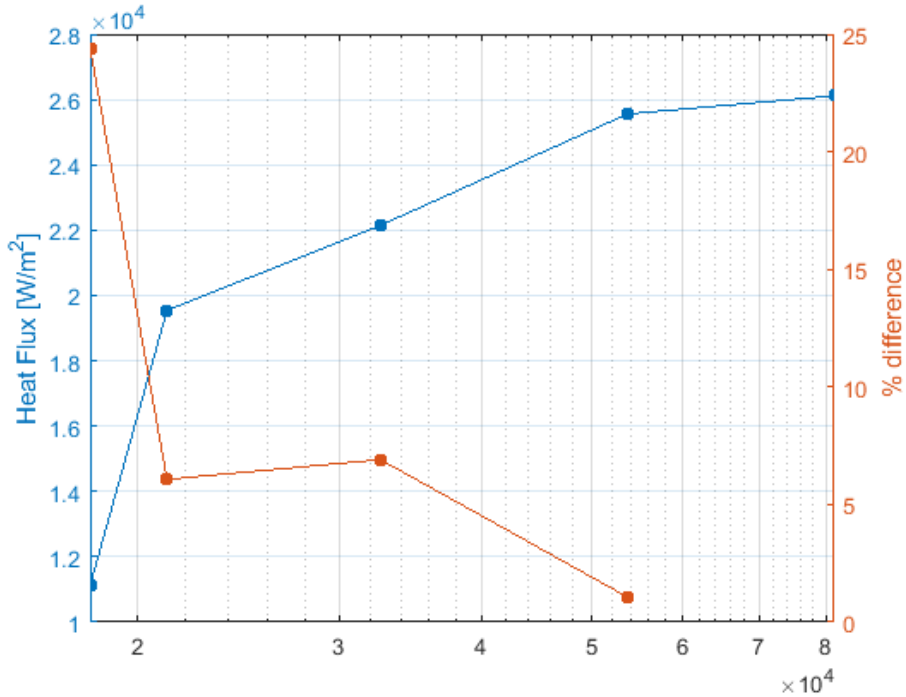


Figure 17. Graph of Mesh Convergence Results for Robotic Arm Physical Studies

## Boundary Conditions

As discussed earlier, the robot is holding a hot object of 500 °C. The heat capacity of the object is unknown, and it is also unknown how long the robot is going to hold the object, the project will consider the object to constant temperature source. For simplicity, only the last link will be used during thermal analysis. The face adjacent to the object will have a constant temperature boundary condition of 500C. The faces that are exposed to ambient air will have convective boundaries with convective heat transfer coefficient  $h = 10\text{W/mK}$  at room temperature which is a realistic value. The faces that are connected to different links will have adiabatic boundaries assuming high contact resistance. To analyze the effect of the effector as a fin, two different geometries will be used during analysis. The image at the right is the geometry link with the fin. The entire boundaries from the fin will be considered as convective boundaries because the surface of effector will be rough so that the heat from the object will not be transferred to the effector.

## Results

For the analysis, two different cases were considered. The first case involved using structural steel without fins, while the second case incorporated the use of fins. The thermal conductivity of the structural steel employed in both cases is 60.5 W/m·K.

Figure 18 illustrates the temperature distribution when using structural steel in a finless geometry. The temperature at the junction where different links connect reaches 403°C. This high

temperature indicates the necessity for thermal insulation material between links if structural steel is used. To simplify the robot's geometry and reduce the interface temperature, further adjustments will be required.

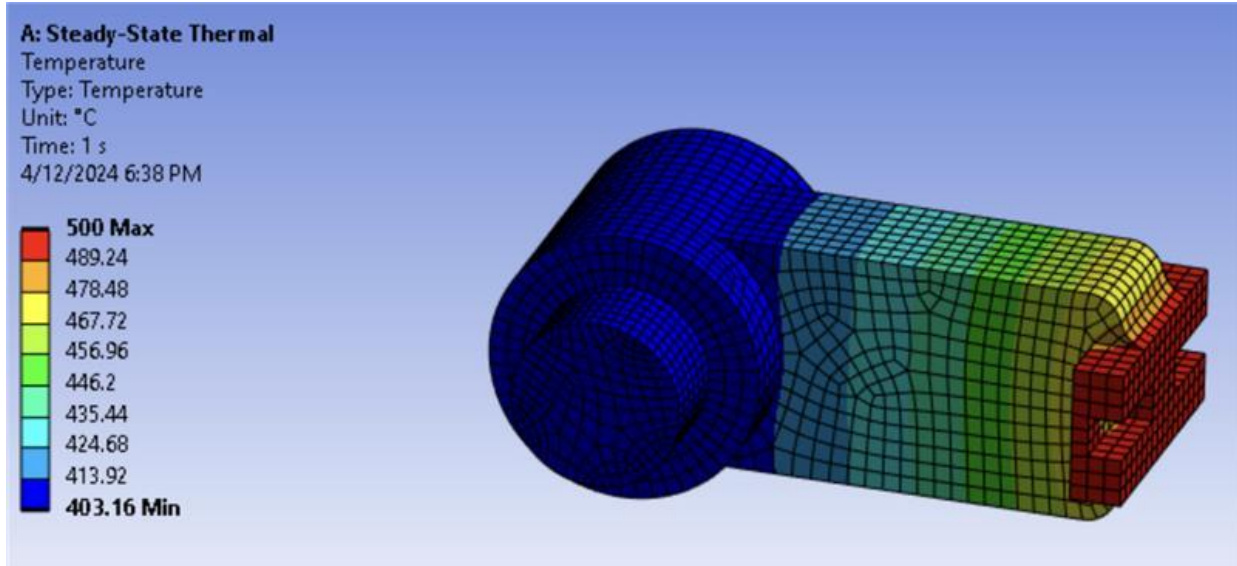


Figure 18. Temperature Distribution in Link 4 Subjected to 500°C at the End Effector, Without Fin.

Figure 19 displays the temperature distribution when fins are incorporated into the design. It shows that the temperature at the edge where different links connect is reduced to 390°C. Although the addition of fins helps to lower the temperature, the effect is not substantial enough to significantly decrease the temperature at the connection points. This modest reduction indicates that the geometry of the link alone does not adequately address the issue of high temperatures at the connections. Consequently, this situation underscores the need for a material substitution to one with lower thermal conductivity. Such a change aims to further decrease the temperature at the connection points, potentially achieving temperatures close to room temperature.

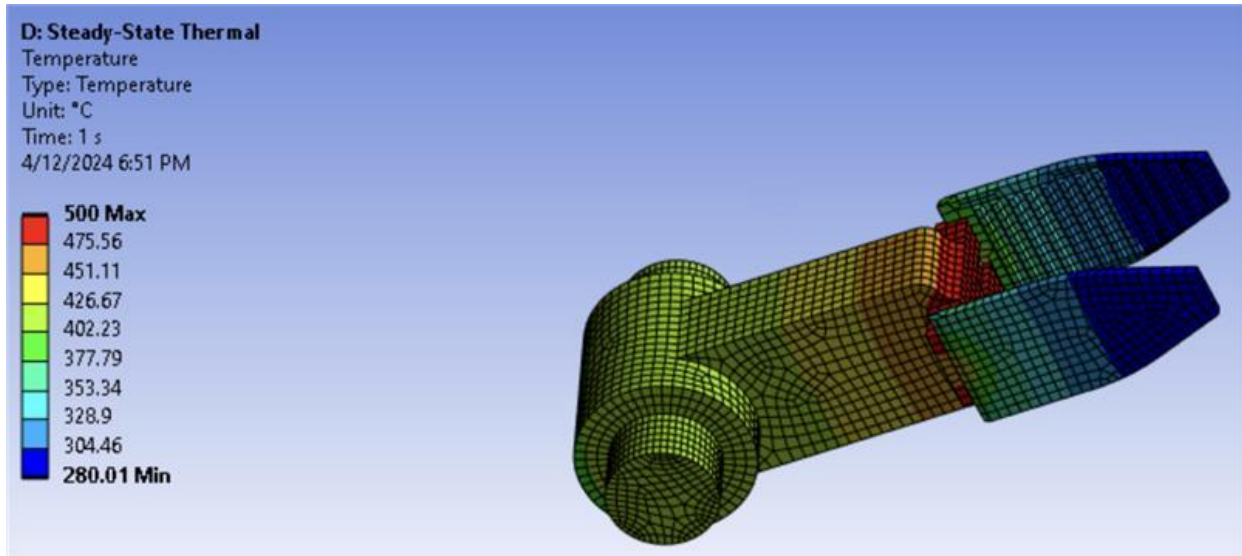


Figure 19. Temperature Distribution in Link 4 Subjected to 500°C at the End Effector, With Fin

## Validation

2D temperature distribution is plotted for verification. It is simplified as plate. As it is shown, one edge is constant temperature, and the other edges are convective boundaries. Overall, it is similar to the distribution of 3D geometry. The temperature of 3D geometry is lower than the 2D due to more exposed area to air, giving more space to dissipate the heat.

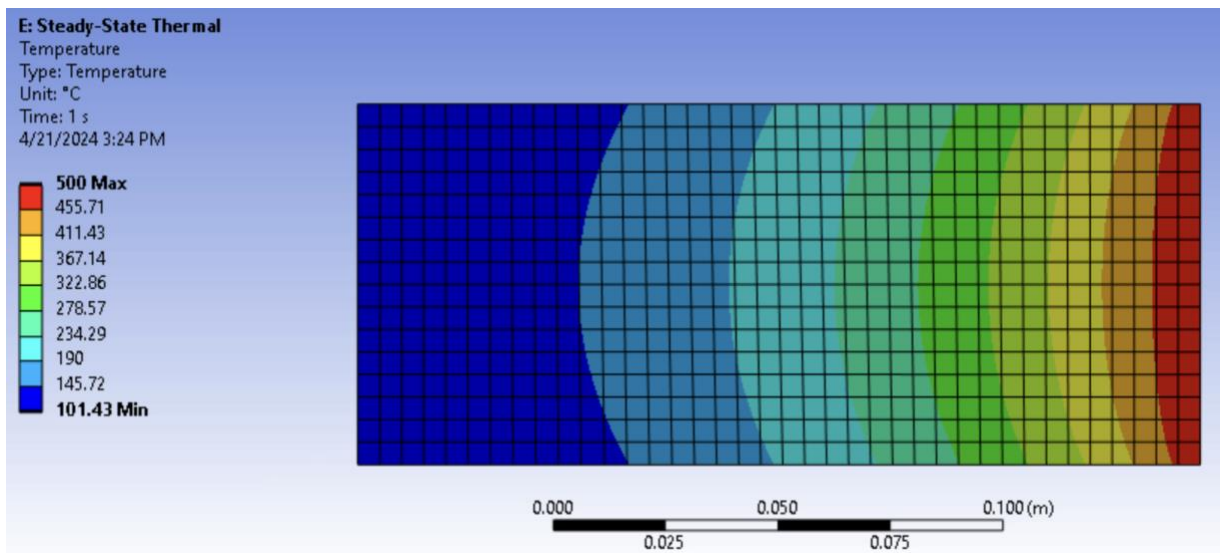


Figure 20. 2D temperature distribution using zirconia

## Design Optimization

In the design optimization section, zirconia has been selected to address the high temperature issues observed with structural steel. Zirconia's thermal conductivity is significantly

lower, approximately 1/30th that of structural steel, while its Young's modulus is comparable to that of structural steel, ensuring that the substitution does not impact the static or dynamic analysis adversely.

Figure 21 illustrates the temperature distribution and heat flux when zirconia is used as the material, without incorporating fins in the design. The temperature at the edges, where different links connect, is 43°C, closely aligning with room temperature as desired. This demonstrates that the choice of material has a more pronounced effect on reducing temperature than changes in geometry alone.

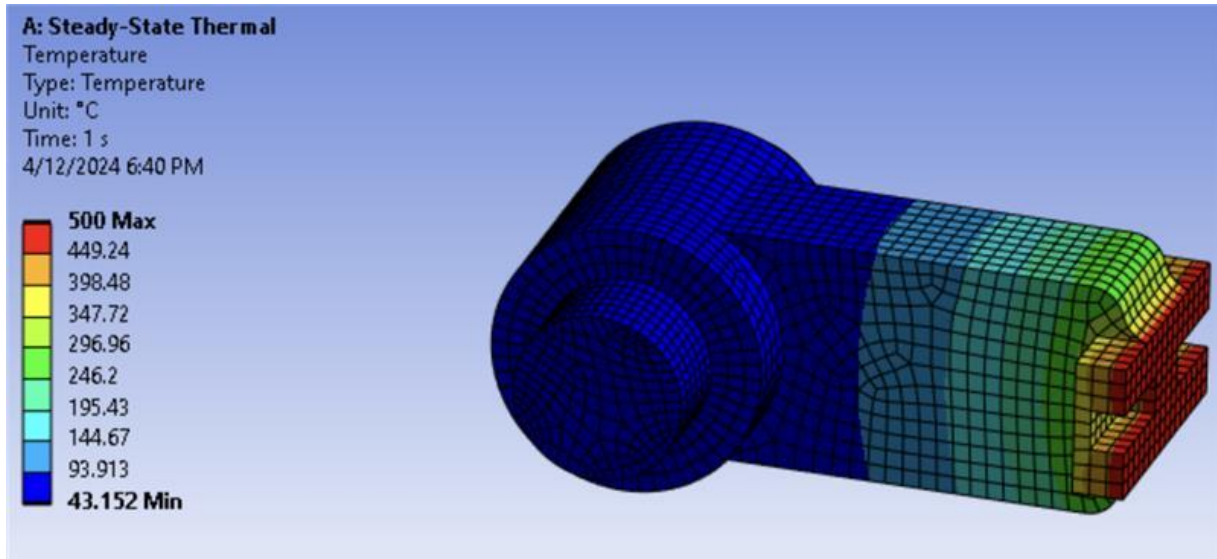


Figure 21. Temperature Distribution in Link 4 Made of Zirconia, Subjected to 500°C at the End Effector, Without Fin

Figure 22 presents the temperature distribution and heat flux when zirconia is used with fin geometry. In this configuration, the temperature at the joint is further reduced to 40°C. The inclusion of fins contributes to this additional decrease in temperature at the connection points, enhancing the overall thermal management of the structure.

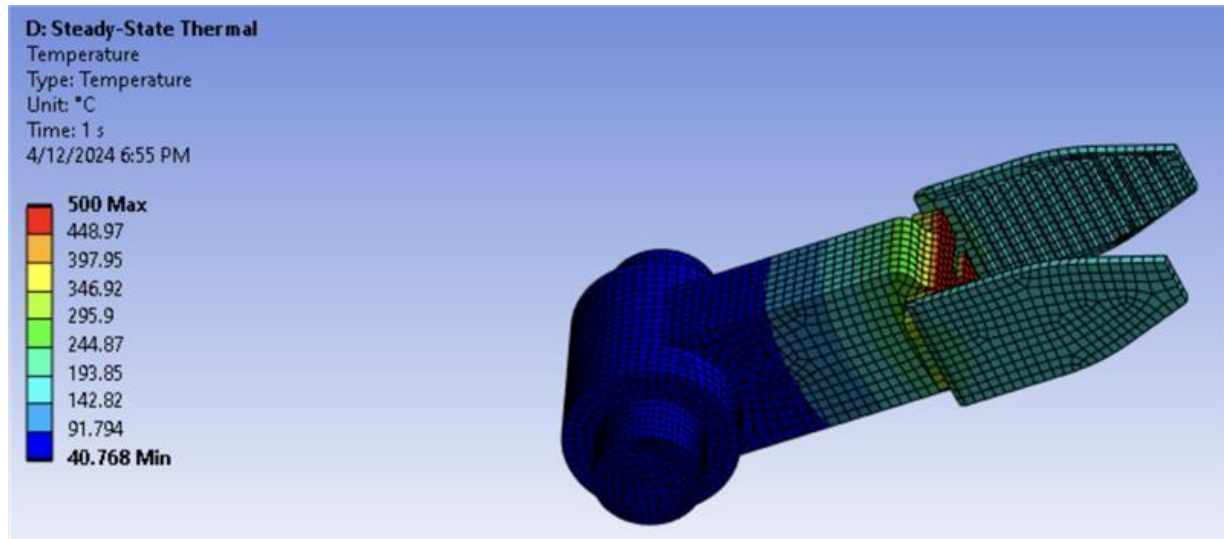


Figure 22. Temperature Distribution in Link 4 Made of Zirconia, Subjected to 500°C at the End Effector, With Fin

In both scenarios, the heat flux at the joint is minimal, constituting only 1% of the heat flux observed at the effector side as shown in Figure 23. This negligible heat flux underscores that thermal effects become inconsequential at the joint when zirconia replaces the top link material. Thus, the use of zirconia not only meets the thermal requirements but also simplifies the thermal management without needing additional design complexities. This optimization significantly enhances the robot arm's performance by reducing thermal risks and maintaining structural integrity.

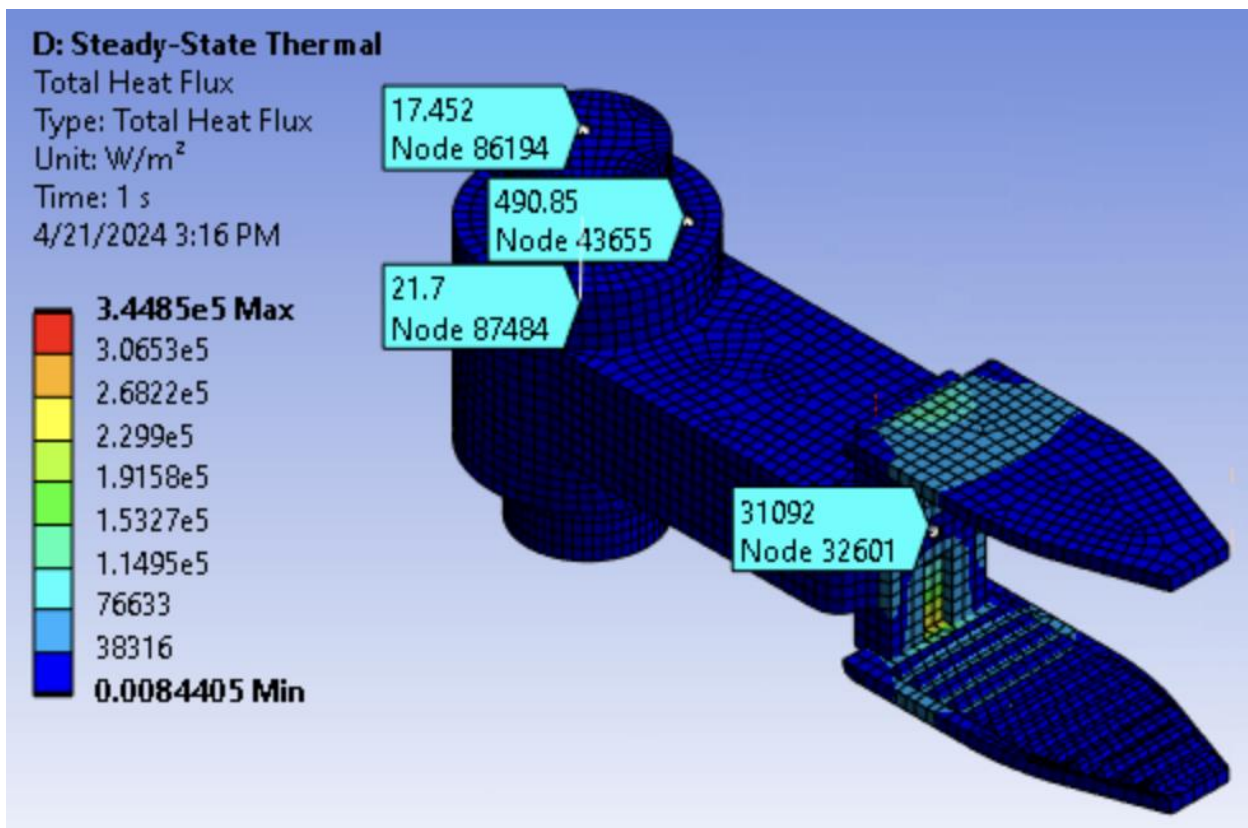


Figure 23. Total Heat Flux Distribution in Link 4 Made of Zirconia, Subjected to 500°C at the End Effector, Without Fin

## VI. Additional Studies

### Dynamic Analysis

For additional analysis, the arm was dynamically analyzed with the same load from static testing. This was done as a further proof of concept and will be used to demonstrate that the robot arm is capable of not only bearing the required load but also lifting it from the 0° orientation to the 90° orientation. The optimized joint two was used – 30 mm hole and silicon carbide. For this analysis, 3 revolute joints were created to capture the degrees of freedom of the arm. Additionally, the two end effector plates were fixed in place to joint 4, preventing any axial movement. Rotational joint loads were applied at each of the three joints: 0° to 90° rotation at joint 1 and 0° rotation at joints 2 and 3. This loading, along with the 2000 N force load, can be seen in Figure 24.

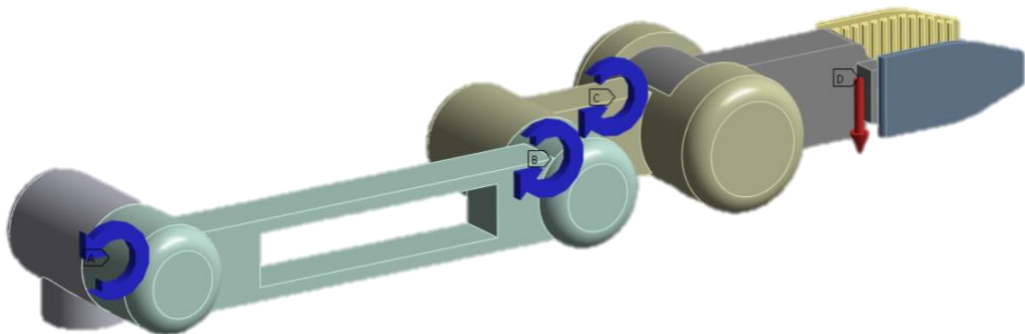


Figure 24. Dynamic Loading of Robot Arm

An 8 mm automatic mesh with linear element order and Quad/Tri free face mesh was generated for the arm, resulting in 20950 elements. Since the stresses in link two are the only necessary values, link 2 was set to flexible, ensuring that it could deform and therefore receive stresses. All other bodies were set to rigid. The generated mesh can be seen in Figure 25.



Figure 25. 8 mm Mesh for Dynamic Analysis

The dynamic model converged correctly. The arm was moved from the 0-degree position to the 90-degree position in increments of 1 angle per second, with the 2000 N load continuously applied in each increment. The motion of the arm with the equivalent (Von Mises) stress displayed can be seen in Figure 26.

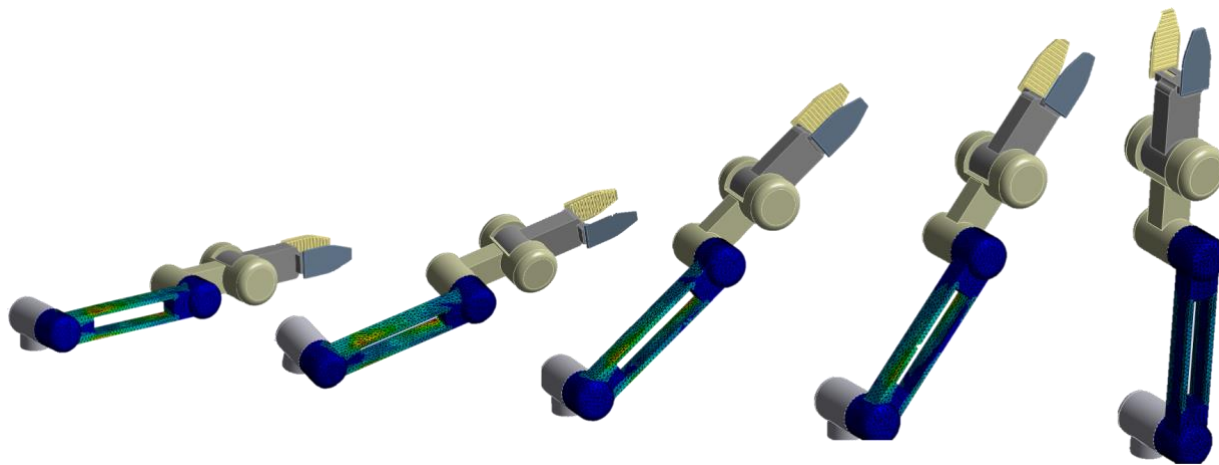


Figure 26. Stress Distribution of Joint Two throughout the Motion of the Arm

The graph of stress over time for link 2 can be seen in Figure 27 and the maximum stress of 149.8 MPa occurred while the arm was at the 0-degree position. This is less than the yield stress of silicon carbide, the material used for link 2 (320 MPa), resulting in a safety factor of 2.18 and ensuring that it will not fail from the dynamic motion of the arm.

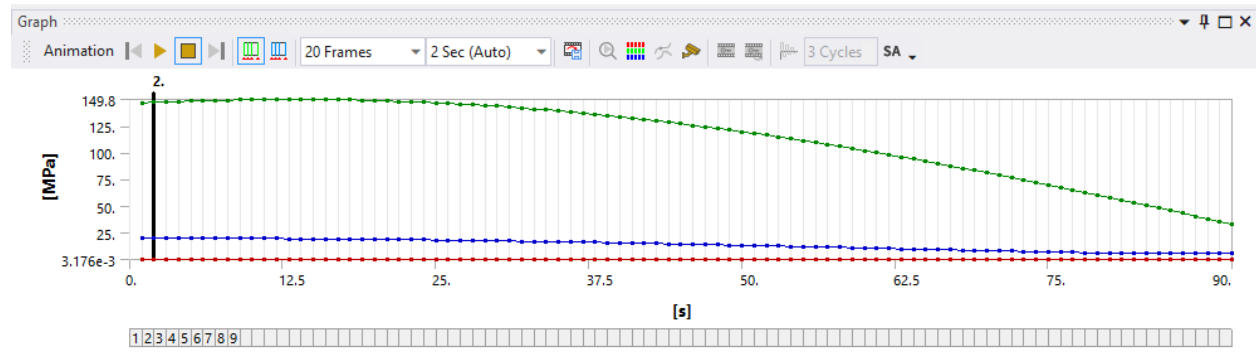


Figure 27. Maximum Stress in Link Two over Time

## Failure Tests

To further assess the capabilities of our selected design, the failure points were determined for the static, dynamic, and thermal analyses. For static and dynamic, this point was determined by incrementally increasing the force applied until the maximum stress exceeded the yield stress of the material. For static analysis, this occurred at 5100 N (Figure 28). This load generated a maximum nodal stress of 322.82 MPa and a maximum elemental stress of 278.81 MPa. The more-accurate elemental stress did not exceed the yield stress of the material (320 MPa), and thus this may not be the actual limit of the design. However, since the nodal stress exceeded the yield stress, this was selected as the failure point to ensure that our design sufficiently accounted for potential inaccuracies in our results.

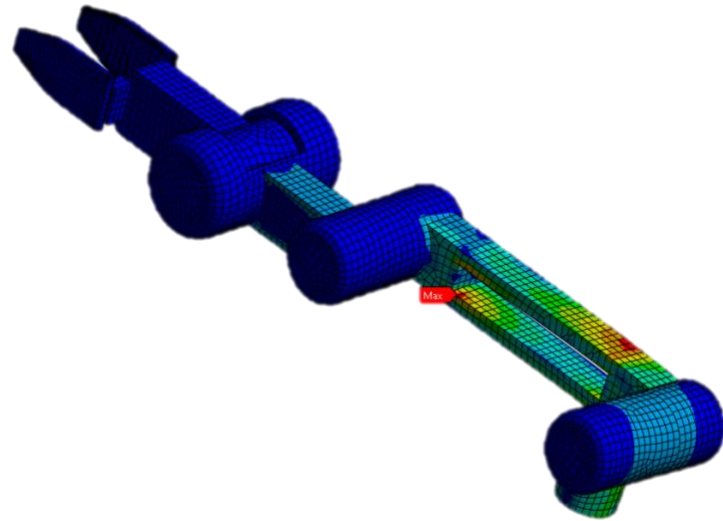


Figure 28. Maximum Static Stress

The arm failed under dynamic analysis at a load of 4500 N (figure 29). This generated a corresponding maximum stress of 340.4 MPa, significantly exceeded the yield stress of the material.

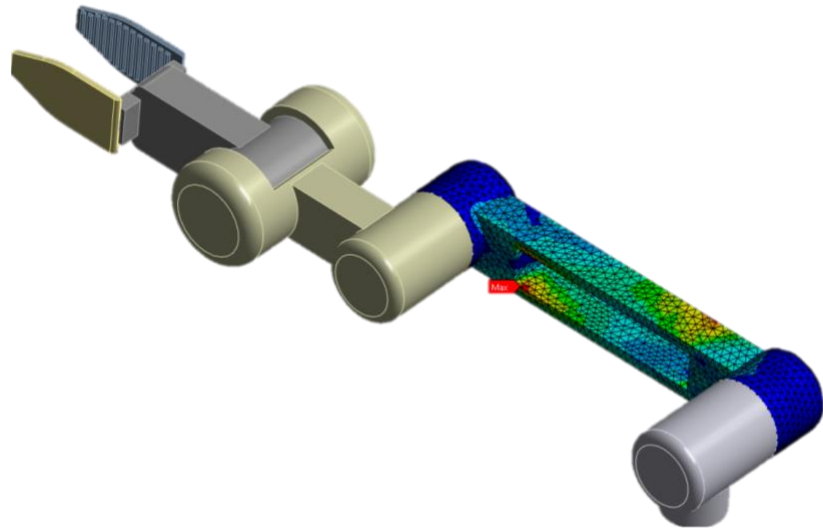


Figure 29. Maximum Dynamic Stress

The thermal failure point was selected by identifying the melting point of zirconia, the selected material for link 4. The melting point of  $2600^{\circ}\text{C}$  was applied to the model in Figure 30, simulating the arm gripping an object at this temperature.

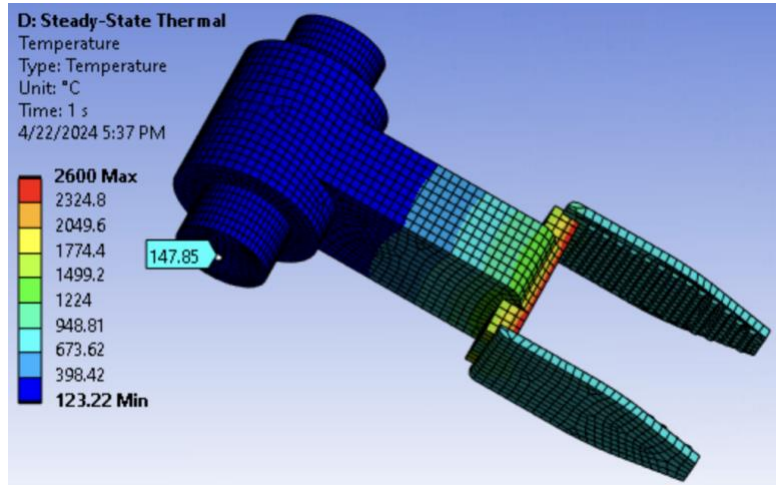


Figure 30. Thermal Limit of Link 4

Based on this analysis, the static, dynamic, and thermal load limits for the optimized design have been identified: 5100 N for static, 4500 N for dynamic, and  $2600^{\circ}\text{C}$  for thermal.

## ***VII. Conclusion***

A robotic arm was developed with overall dimensions under 1 meter, capable of lifting and transporting an object weighing 200 kg and a temperature of  $500^{\circ}\text{C}$ . This arm was optimized by applying a material of silicon carbide and introducing a 30 mm x 200 mm hole in the second linkage. These changes optimized the overall weight of the arm and strength of the linkages. Zirconia was applied to the fourth linkage due to its low thermal conductivity for handling hot materials and its relative strength. Across all of these analyses, a safety factor of at least 2 was achieved, demonstrating that the arm is sufficient for use under the prescribed loading.

## ***VIII. Future Work***

For future analyses, the integration of motor specifications at the joints could be explored to design motors capable of delivering the necessary torque for lifting the specified loads. This enhancement would align the robotic arm's design more closely with real-world applications, serving as a critical step toward operational deployment. Additionally, the complexity of robot arm designs could be increased. While the 3R robot serves basic functions, many industrial applications demand more sophisticated configurations that include pneumatic joints or rotations around additional axes.

Further, more intricate loading conditions could be examined. The arm's longevity could be assessed through fatigue analysis using the current loading method. Additionally, fracture

analysis could be conducted to determine the exact failure modes of the arm under maximum load conditions. Based on these findings, design modifications could be proposed to further optimize the robot, enhancing both its performance and durability.

## IX. Project Proposal

### Fatigue Analysis on the Robot Arm

Team 1: Kad Kook, Zack Burkhardt, Min-Geun Park

#### Introduction

The increasing complexity and functionality of robotic systems have led to significant advancements in the design and development of robotic arms. However, these robotic arms' design poses considerable challenges, especially in structural integrity, reliability under load, and operational efficiency. This project aims to utilize Finite Element Analysis (FEA) to investigate the structural performance of a robot arm, focusing on its ability to withstand operational stresses, vibrations, and potential material fatigue over its service life. By applying the principles of FEA, we will assess the mechanical properties of the robot arm, including stress distribution, deformation, and the potential for failure in critical components. This comprehensive analysis will not only highlight areas vulnerable to failure but also provide valuable data for optimizing the design for enhanced durability and efficiency. Through a detailed examination of the finite element model, coupled with real-world and analytical validation, this analysis will provide a solid foundation for future innovations in robotic arm technology.

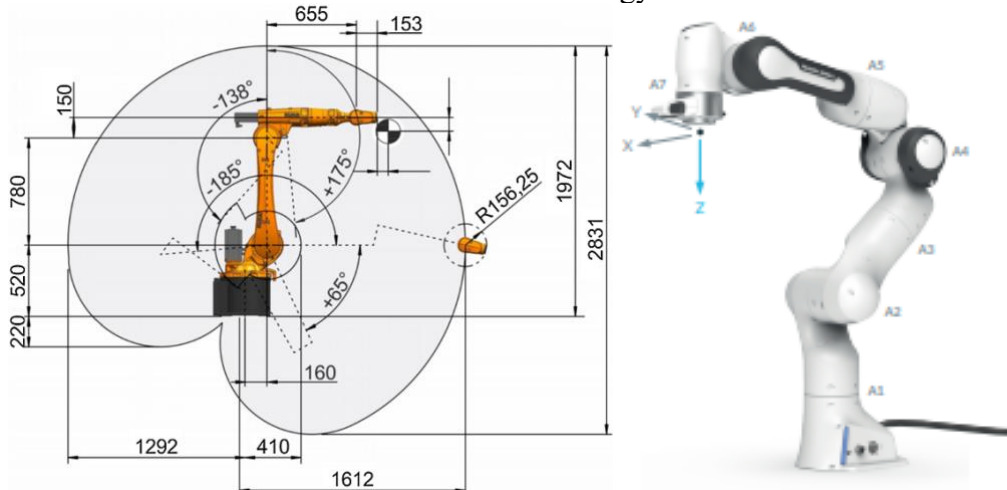


Figure 1. Example dimensions/structure of robot arm

#### Proposed Analysis

This project will focus on stress distribution, deformation, and material fatigue under operational conditions. Through detailed modeling in FEA software, the arm will undergo static and dynamic load analyses to identify stress concentrations and potential failure points, alongside material fatigue analysis. Various materials will be evaluated for their suitability, with the aim of optimizing the arm's design for improved strength, durability, and efficiency. Real-world and analytical validation will compare FEA predictions with experimental data to refine the model, ensuring its accuracy.

## Expected Results

The report will examine the effects of punched holes on the upper arm of the robot. The arm's weight will decrease as the number and size of holes increase, but there will be a higher stress concentration. The robot's maximum load will be the function of the number of holes, and size of the hole, and it will also affect the robot arm's weight. By running multiple cases, it will be possible to obtain the relation between those. There will be an appropriate hole and number of holes that can optimize the robot arm in terms of its weight and the maximum load.

## Proposed Validation Methods

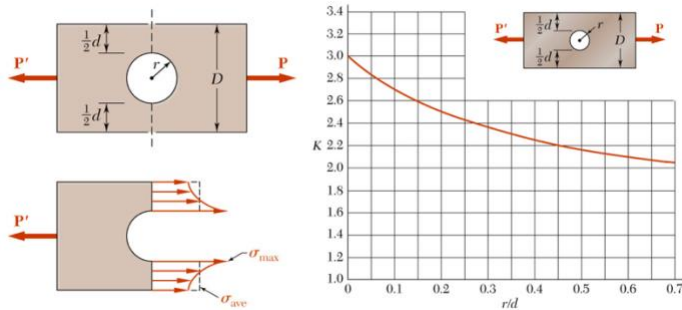


Figure 2. Analytical model of a single hole

Analytic calculation and simplified simulation will be used to verify the simulation. Stress concentration factor shows the maximum stress on the cross section when there is circle shaped vacancy in the middle of the bar. By simplifying the robot arm structure, it is possible to get an analytic solution. When the distance between holes is so close that the assumption that each hole will not affect to one another, it is possible to run a simple case in a simulation and compare with our exact cases, verifying that the exact result is not very deviated from the simplified one.

## Material/geometry/loading modification/optimization

Numerous changes could be made to the robot arm to further change the results of the analysis. The material could be changed to carbon fiber, as this is another material used by KUKA. Naturally, this would affect the strength and weight of the material, and consequently could allow for different hole patterns than found with the aluminum arm. More complex arm geometries could be tested, as the forces will distribute differently throughout the arm.

## **X. References**

- [1] B. Chen et al., “Smart Factory of Industry 4.0: Key Technologies, Application Case, and challenges,” *IEEE Access*, vol. 6, pp. 6505–6519, 2018. doi:10.1109/access.2017.2783682
- [2] nd, “KR 4 AGILUS”, accessed April 23 2024, <https://www.kuka.com/en-us/products/robotics-systems/industrial-robots/kr-4-agilus>
- [3] nd, “KR QUANTEC”, accessed April 23, 2024, <https://www.kuka.com/en-us/products/robotics-systems/industrial-robots/kr-quantec>
- [4] C. A. My, C. H. Le, M. Packianather, and E. L. J. Bohez, “Novel robot arm design and implementation for Hot Forging Press Automation,” *International Journal of Production Research*, vol. 57, no. 14, pp. 4579–4593, Sep. 2018. doi:10.1080/00207543.2018.1521026